Chinese Chemical Letters 37 (2026) 110977

Contents lists available at ScienceDirect

Chinese Chemical Letters

journal homepage: www.elsevier.com/locate/cclet

In vivo second near-infrared fluorescence and ratiometric photoacoustic dual-modality imaging of glutathione

Yu Zhang, Shan Lei, Yuantao Pan, Chao Zhao, Qiang Liu, Yumeng Wu, Yurong Liu, Meng Li, Peng Huang, Jing Lin*

Marshall Laboratory of Biomedical Engineering, International Cancer Center, Laboratory of Evolutionary Theranostics (LET), School of Biomedical Engineering, Shenzhen University Medical School, Shenzhen University, Shenzhen 518055, China

ARTICLE INFO

Article history:
Received 25 November 2024
Revised 15 February 2025
Accepted 19 February 2025
Available online 19 February 2025

Keywords:
Glutathione
In vivo
Second near-infrared dye
Fluorescence imaging
Ratiometric photoacoustic imaging

ABSTRACT

The level of glutathione (GSH) is significantly associated with numerous pathological processes, thus, real-time detection of the GSH level is of significance for early diagnosis of GSH-related diseases. Herein, we developed *in vivo* second near-infrared (NIR-II) window fluorescence (FL) and ratiometric photoacoustic (RPA) dual-modality imaging of GSH using a GSH-activatable probe (LET-14). LET-14 was synthesized based on a rhodamine hybrid xanthene skeleton with a FL shielding 2,4-dinitrobenzene sulfonyl group that can be specifically cleaved by GSH, thus resulting in a markedly bathochromic-shift absorption, a 6.5-fold increase in NIR-II FL intensity (FL_{920}) and a 13-fold increase in RPA signal (PA_{880}/PA_{705}) *in vitro*. Intriguingly, LET-14 exhibits good selectivity and sensitivity for NIR-II FL and RPA dual-modality imaging of GSH in 4T1 tumor-bearing mouse model. Our findings develop an *in vivo* detection tool of GSH, which has great potential in the field of cancer diagnosis.

© 2025 Published by Elsevier B.V. on behalf of Chinese Chemical Society and Institute of Materia Medica, Chinese Academy of Medical Sciences.

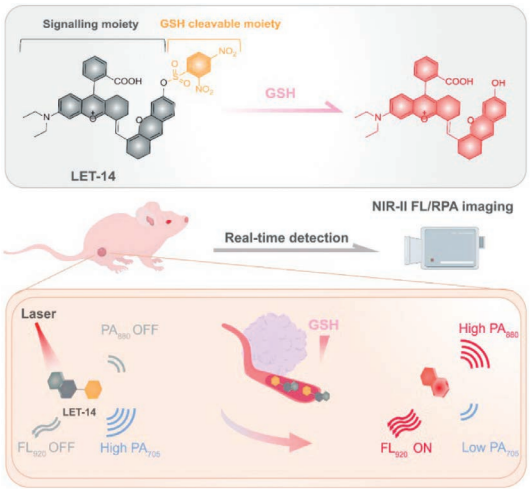
Glutathione (GSH), a tripeptide thiol, assumes a pivotal position in sustaining cellular redox homeostasis and safeguarding cells against oxidative stress [1]. The level of GSH is significantly associated with numerous pathological processes, including cancers, Alzheimer's disease, neurodegenerative disorders and a plethora of other diseases [2–5]. GSH is regarded as an important biomolecule for diagnosis of various diseases. For instance, the GSH content in tumor tissues is no less than fourfold higher compared to that in normal tissues [6–9]. Consequently, real-time detection of GSH levels is important for the early diagnosis of GSH-associated diseases, especially for cancers.

Currently, visualization of *in vivo* GSH is based on fluorescence (FL) probes in visible or first near-infrared (NIR-I) window [10–20]. However, FL imaging in these windows is circumscribed by factors like insufficient tissue penetration depth and photon scattering, which conspicuously hinders its employment in highly sensitive imaging of GSH *in vivo*. Noticeably, FL imaging in second NIR (NIR-II) window possesses the capability to markedly alleviate the impact of light scattering phenomena and autofluorescence effects, thereby allowing for deeper tissue penetration depths and enhanced spatial resolution [21–28]. The advancement of NIR-II FL probe for *in vivo* GSH imaging is a hotspot [23,29]. Nonetheless, single imaging modality usually suffers deficient accuracy or quantification [30–33]. On account of this, photoacoustic (PA) imaging serves as a robust complement to NIR-II FL imaging for the detection of GSH, offering more comprehensive and precise detection outcomes. The PA imaging offers exceptional deep tissue penetration, reaching depths of several centimeters, along with high 3-dimensional (3D) spatial resolution imaging capabilities for living subjects. However, to date, the applications of most reported PA probes for GSH detection have been significantly constrained by various endogenous biomolecules. Furthermore, this type of probes was dependent on the single-channel signal variation of PA imaging and was prone to the influence of multiple environmental factors, for instance, microenvironmental disparities and diverse photobleaching rates [34,35]. By contrast, the ratiometric photoacoustic (RPA) probe effectively surmounts the numerous constraints of single-channel imaging probes through the introduction of self-calibration properties, thereby enabling more accurate detection of GSH [36–43]. Taken together, the development of NIR-II FL/RPA imaging with self-calibration capabilities is urgently required for the accurate diagnosis of GSH *in vivo*.

Herein, we developed *in vivo* NIR-II FL/RPA dual-modality imaging of GSH using a GSH-activatable probe (denoted as LET-14) (Scheme 1). LET-14 consisted of a rhodamine hybrid xanthene skeleton bridged with a shielding 2,4-dinitrobenzene sulfonyl (DNBS) group, which could be specifically cleaved by GSH,

* Corresponding author.
E-mail address: jingl@szu.edu.cn (J. Lin).

https://doi.org/10.1016/j.cclet.2025.110977
1001-8417/© 2025 Published by Elsevier B.V. on behalf of Chinese Chemical Society and Institute of Materia Medica, Chinese Academy of Medical Sciences.



Scheme 1. Schematic illustration of an activatable NIR-II FL and RPA dual-modality probe (LET-14) for *in vivo* GSH imaging.

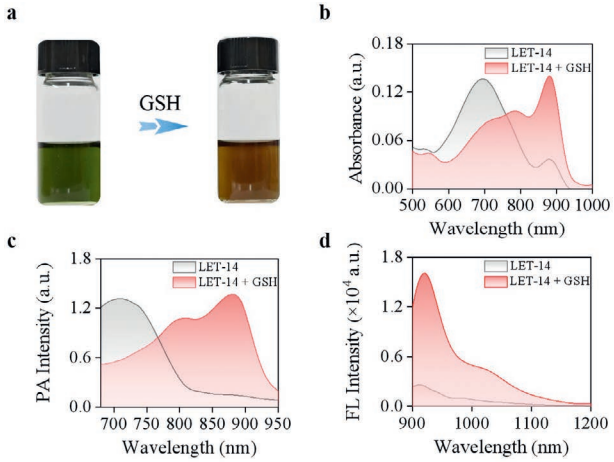


Fig. 1. (a) Color change of LET-14 towards GSH. (b) UV–vis-NIR absorption, (c) PA spectra, and (d) NIR-II FL (λ_{ex} = 880 nm) of LET-14 (10 μmol/L) after incubation with/without GSH (50 μmol/L) for 30 min in dimethyl sulfoxide (DMSO)/phosphate buffered saline (PBS) (v/v = 2/3, pH 7.4).

resulting in a markedly bathochromic-shift absorption, a 6.5-fold increase in NIR-II FL intensity (FL_{920}) and a 13-fold increase in RPA signal (PA_{880}/PA_{705}). *In vitro* and *in vivo* experiments demonstrated that LET-14 could selectively and sensitively identify GSH using NIR-II FL/RPA dual-modality imaging, which is a promising diagnostic tool.

LET-14 was synthesized by an aldol condensation reaction of rhodamine-type fluorophore with xanthene derivative (Fig. S1 in Supporting information). The structures of LET-14 and intermediates have been characterized by nuclear magnetic resonance (NMR) and electrospray ionization mass spectra (ESI-MS) (Figs. S2–S10 in Supporting information). LET-14 is ensconced in a "fluorescence caged" status, due to the shielding impact of DNBS on the intramolecular charge transfer (ICT) process. In the presence of GSH, a thiol-promoted cleavage reaction takes place between GSH and DNBS, leading to the liberation of LET-14 from the caged moiety, thereby simultaneously turning on the NIR-II FL and RPA signals for imaging of GSH (Scheme 1). The mechanism of the cleavage reaction between LET-14 and GSH was further validated by time-dependent ^{1}H NMR and ESI-MS (Figs. S11 and S12 in Supporting information).

The photophysical properties of LET-14 were tested before and after addition of GSH. After incubating with GSH (50 μmol/L) for 30 min, the LET-14 (10 μmol/L) showed a noticeable color change from green to brown, visible by the naked eye (Fig. 1a). At the same time, the absorption band of LET-14 manifested red-shift ranging from 695 (Abs_{695}) to 880 nm (Abs_{880}) (Fig. 1b). The properties of the ultraviolet-visible-near infrared (UV–vis-NIR) absorption spectroscopy impelled us to further explore its PA property. As shown in Fig. 1c, upon the addition of GSH, the PA signal shifted from 705 nm to 880 nm, and this change was in accordance with the results of the UV–vis-NIR absorption spectra. Concurrently, a significant enhancement of NIR-II FL emission at 920 nm (FL_{920}) was observed after incubation with GSH (Fig. 1d), which demonstrated that LET-14 exhibited an excellent response to GSH.

Next, the concentration and response time-dependent spectral variations were demonstrated for the assessment of sensitivity of LET-14 to GSH. The Abs_{880} intensity of LET-14 exhibited a gradual increase, while that of the Abs_{695} demonstrated a decrease as various concentrations of GSH addition (0–50 μmol/L) (Fig. 2a). The FL_{920} intensity gradually intensified and reached its peak value at 50 μmol/L, with a nearly 6.5-fold signal enhancement (Fig. 2b). Furthermore, a significant linear correlation (R^2 = 0.9958) was observed between the FL_{920} intensity and GSH concentration (Fig.

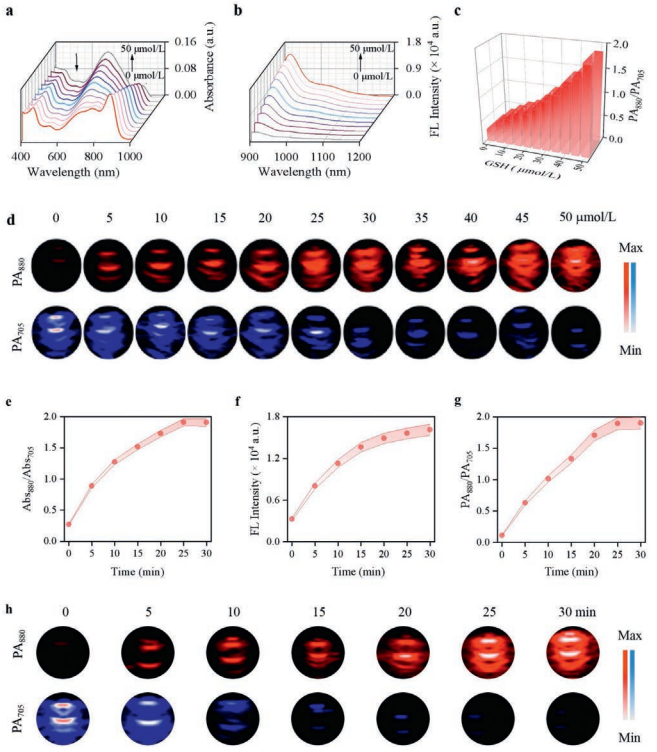


Fig. 2. (a) UV–vis-NIR absorption, (b) NIR-II FL spectra (λ_{ex} = 880 nm), (c) the ratio of PA_{880}/PA_{705} intensity and (d) the corresponding PA images of LET-14 (10 μmol/L) with the addition of GSH (0–50 μmol/L) for 30 min in DMSO/PBS (v/v = 2/3, pH 7.4). Time-dependent (e) Abs_{880}/Abs_{695} intensity, (f) NIR-II FL_{920} intensity (λ_{ex} = 880 nm), (g) PA_{880}/PA_{705} intensity and (h) the corresponding PA images of LET-14 after incubation with GSH (50 μmol/L) for 30 min in DMSO/PBS (v/v = 2/3, pH 7.4).

S13 in Supporting information), and the detection limit was ascertained to be 0.32 μmol/L. Inspired by the property of the absorption spectrum in the response process between LET-14 and GSH, the PA signal of LET-14 to GSH was also examined. After addition of GSH, the PA_{880} signal exhibited significant enhancement, whereas PA_{705} signal was decreased, thus the signal ratio of PA_{880}/PA_{705} received a 13-fold increase (Figs. 2c and d). The above results indicated that LET-14 could detect GSH using both FL and RPA imaging. Besides, the kinetics reaction of LET-14 with GSH was investigated. Upon the addition of GSH (50 μmol/L) to LET-14 (10 μmol/L), the

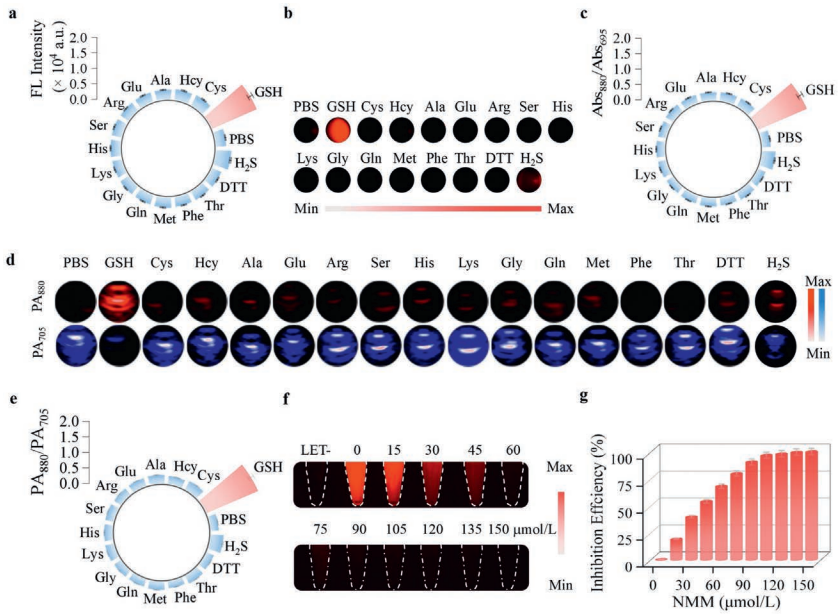


Fig. 3. (a) NIR-II FL_{920} intensity, (b) NIR-II FL images, (c) Abs_{880}/Abs_{695}, (d) PA_{880}/PA_{705} ratio and (e) the corresponding PA images of LET-14 (10 μmol/L) after incubation with various amino acids and hydrogen sulfide for 30 min in DMSO/PBS (v/v = 2/3, pH 7.4). (f) NIR-II FL images of LET-14 (10 μmol/L) with the addition of GSH (50 μmol/L) before incubation with different concentrations of NMM (0-150 μmol/L). (g) The corresponding NIR-II FL_{920} inhibition efficiency. Data are presented as mean ± standard deviation (SD) ($n = 3$).

Abs_{880}/Abs_{695} ratio displayed a gradual increment over time, attaining a plateau approximately 30 min (Fig. 2e and Fig. S14a in Supporting information). The FL_{920} displayed a similar trend (Fig. 2f and Fig. S14b in Supporting information). Additionally, the ratio of PA_{880}/PA_{705} increased gradually over time, peaked within 30 min, and remained stable thereafter (Figs. 2g and h).

To assess specific response of LET-14 to GSH, we evaluated the reactivity of LET-14 with a variety of biological substances, including L-cysteine (Cys), L-homocysteine (Hcy), L-alanine (Ala), L-glutamic acid (Glu), L-arginine (Arg), L-serine (Ser), L-histidine(His), L-lysine hydrate (Lys), glycine (Gly), L-glutamine (GIn), L-methionine (Met), L-phenylalanine (Phe), L-threonine (Thr), L-dithiothreitol (DTT), hydrogen sulfide (H_2S). As shown in Fig. 3a, GSH was the only species that induced a significant alteration in FL_{920} signal, whereas the other species scarcely brought about any alterations in FL emission of LET-14, which was in line with the outcomes of NIR-II FL images (Fig. 3b). Meanwhile, upon the addition of GSH, a significant alteration in the ratios of Abs_{880}/Abs_{695} (Fig. 3c) and PA_{880}/PA_{705} (Figs. 3d and e) was observed in LET-14, whereas negligible variation in other substances. It is noteworthy that stability is one of the crucial indicators for assessing the quality of FL probes. LET-14 exhibited excellent chemical stability in the presence of reactive oxygen and nitrogen species (RONS), such as H_2O_2 and $ONOO^-$ (Fig. S15 in Supporting information). Additionally, GSH inhibition study was demonstrated by pretreatment with an inhibitor, *N*-methylmaleimide (NMM). As increase of NMM concentration, the inhibition efficiency of LET-14 by GSH was significantly increased, and reached to 100 % at 150 μmol/L of NMM (Figs. 3f and g). These results demonstrated that LET-14 exhibited high selectivity and rapid responsiveness toward GSH.

After validating the outstanding FL and PA properties of LET-14 for detection of GSH, we conducted a systematic investigation into the biocompatibility for *in vitro* imaging. First, the biocompatibility of LET-14 was investigated on normal cell line (HEK293T cell) and mouse breast cancer cell line (4T1 cell). After 24 h of incubation with various concentrations of LET-14 (0–40 μmol/L), all cell viabilities were over 90 %, indicating its good biocompatibility (Figs. 4a and b). Subsequently, cell imaging experiments were conducted by NIR-II FL/PA imaging system (Fig. 4c). When 4T1 cells were incubated with LET-14, the NIR-II FL signal of cells gradually intensified over time, ultimately reaching a stable state within 2 h. This observation suggested that LET-14 could be efficiently taken up by 4T1 cells and then triggered by endogenous GSH to generate NIR-II FL signals in a time-dependent manner (Figs. 4d and e). By contrast, the NIR-II FL intensity of the cells in NMM-pretreated group remained at a low level, owing to the suppressive impact

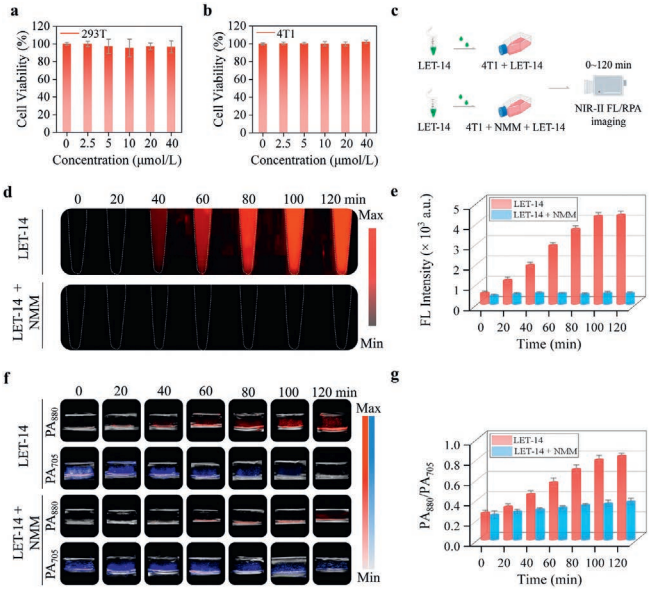


Fig. 4. Cell viability estimated by MTT assay with HEK293T (a) and 4T1 (b) cells, which were cultured in the presence of LET-14 (0–40 μmol/L) for 24 h. (c) Schematic representation of NIR-II FL and RPA imaging for 4T1 cells. (d) Time-dependent NIR-II FL images of 4T1 cells with/without NMM pretreatment (0.5 mmol/L), respectively, then addition of LET-14 and (e) the corresponding quantitative FL intensity in (d). (f) Time-dependent PA images of 4T1 cells with/without NMM pretreatment (0.5 mmol/L), respectively, then addition of LET-14 and (g) the corresponding quantitative RPA intensity in (f). Data are presented as mean ± SD ($n = 3$).

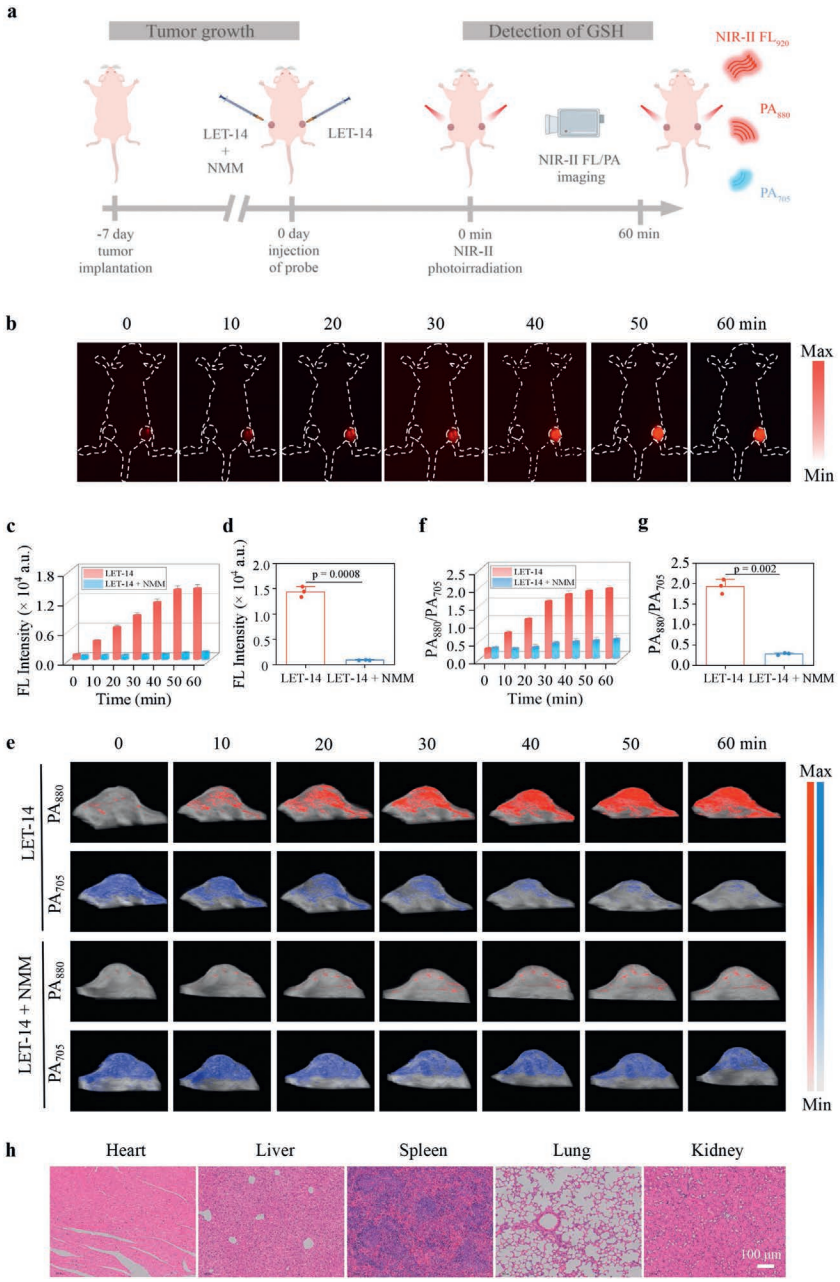


Fig. 5. (a) Schematic representation of NIR-II FL and RPA imaging for 4T1 tumors. (b) Time-dependent NIR-II FL images of 4T1 tumor-bearing nude mice with or without NMM (1 mmol/L, 50 μL), respectively, then injection of LET-14. (c) The relative FL intensity of tumors collected from (b). (d) Quantification of FL intensity of tumors at 60 min ($P = 0.0008$). (e) *In vivo* PA images of 4T1 tumor-bearing nude mice. (f) RPA signal of PA_{880}/PA_{705} measured as a function of post-injection time. (g) Quantification of RPA signals of tumors at 60 min ($P = 0.002$). (h) H&E stained images of major organs (heart, liver, spleen, lung, and kidney) were obtained from mice 14 days post-injection of LET-14 (scale bar: 100 μm). Data are presented as mean ± SD ($n = 3$).

of NMM on GSH activity. Meanwhile, the PA_{705} intensity of cells gradually decreased over time, while that of PA_{880} gradually increased, and finally RPA reached relative stability within 2 h, which was notably higher than that of NMM-pretreated 4T1 cells (2.2-fold) (Figs. 4f and g). These results indicated that LET-14 could be used to monitor intracellular GSH levels through NIR-II FL and RPA dual-modality imaging.

Finally, we further employed LET-14 for NIR-II FL/RPA imaging of GSH in bilateral 4T1 tumor-bearing nude mice (Fig. 5a). All of the *in vivo* experiments were conducted in consistence with the approved protocol of Animal Ethics and Welfare Committee of Shenzhen University (AEWC-SZU). NMM was injected into the left tumor tissue, then LET-14 (0.5 mmol/L, 20 μL) was administered into the tumor tissues on both sides. The NIR-II FL intensity of the tumor (right side) gradually augmented (Fig. 5b), reaching the maximum intensity within 1 h (Fig. 5c), exhibiting an 8-fold enhancement when compared to tumor (left side) pretreated with NMM (Fig. 5d). As shown in Fig. 5e, upon injection of LET-14 into tumor tissues, the PA_{705} exhibited a relatively strong intensity, whereas the PA_{880} was comparatively weak. Interestingly, with the extension of time, the PA_{705} gradually diminished and PA_{880} gradually intensified, ultimately generating a strong RPA signal within 1 h, which was 2.5-fold higher than that of tumor (left side) pretreated with NMM (Figs. 5f and g). Taken together, these results demonstrated LET-14 with high sensitivity for GSH detection *in vivo* through NIR-II FL and RPA dual-modality imaging.

Furthermore, the biocompatibility of LET-14 was also evaluated *in vivo*. As shown in Fig. 5h, the hematoxylin and eosin (H&E) stained images of major organs (heart, liver, spleen, lung, kidneys) showed no distinct organ damage or inflammation after LET-14 treatment for 14 days, indicating its good biocompatibility.

In summary, we have developed a GSH-activatable dual-modality probe (LET-14) that integrated NIR-II FL and RPA imaging abilities for *in vivo* GSH detection. Experimental results demonstrated that LET-14 can be specifically and sensitively activated by GSH, leading to significant enhancement of NIR-II FL and RPA signals, being capable of effectively differentiating between GSH and closely related biothiols like Cys and Hcy. Importantly, LET-14 showed good biocompatibility and achieved accurate and reliable *in vivo* GSH monitoring by leveraging the complementary advantages of NIR-II FL/PA dual-modality imaging. Taken together, LET-14 showed substantial potential for *in vivo* detection of GSH-related diseases.

Declaration of competing interest

The authors declare that they have no known competing financial interests or personal relationships that could have appeared to influence the work reported in this paper.

CRediT authorship contribution statement

Yu Zhang: Writing – original draft, Methodology, Investigation, Data curation. **Shan Lei:** Writing – review & editing, Formal analysis. **Yuantao Pan:** Investigation, Data curation. **Chao Zhao:** Writing – original draft, Data curation. **Qiang Liu:** Data curation. **Yumeng Wu:** Data curation. **Yurong Liu:** Data curation. **Meng Li:** Data curation. **Peng Huang:** Writing – review & editing. **Jing Lin:** Writing – review & editing, Supervision, Funding acquisition, Conceptualization.

Acknowledgments

This work was financially supported by the National Natural Science Foundation of China (Nos. 82372116, U23A2097), Guangdong Basic and Applied Basic Research Foundation (No. 2022A1515010620), Shenzhen Medical Research Fund (Nos. B2302047, A2302047), and Shenzhen Science and Technology Program (No. JCYJ20220818095806014) and Research Team Cultivation Program of Shenzhen University (No. 2023QNT019). The authors thank instrumental Analysis Center of Shenzhen University.

Supplementary materials

Supplementary material associated with this article can be found, in the online version, at doi:10.1016/j.cclet.2025.110977.

References

[1] K. Umezawa, M. Yoshida, M. Kamiya, T. Yamasoba, Y. Urano, Nat. Chem. 9 (2017) 279–286.
[2] J. Zhou, P. Jangili, S. Son, et al., Adv. Mater. 32 (2020) 2001945.
[3] Y. Xiong, C. Xiao, Z. Li, X. Yang, Chem. Soc. Rev. 50 (2021) 6013–6041.
[4] B.D. Paul, Front. Aging Neurosci. 13 (2021) 659402.
[5] Y. Wang, H. Yan, Y. Yue, et al., Chem. Eng. J. 464 (2023) 142496.
[6] H. Fan, Z. Guo, Coordin. Chem. Rev. 480 (2023) 215027.
[7] G.K. Balendiran, R. Dabur, D. Fraser, Cell Biochem. Funct. 22 (2004) 343–352.
[8] M.P. Gamcsik, M.S. Kasibhatla, S.D. Teeter, O.M. Colvin, Biomarkers 17 (2012) 671–691.
[9] B. Niu, K. Liao, Y. Zhou, et al., Biomaterials 277 (2021) 671–691.
[10] X. Jiang, J. Chen, A. Bajic, et al., Nat. Chem. 8 (2017) 16163.
[11] S. Lee, J. Li, X. Zhou, J. Yin, J. Yoon, Coordin. Chem. Rev. 366 (2018) 29–68.
[12] S. Mo, X. Zhang, S. Hameed, Y. Zhou, Z. Dai, Theranostics 10 (2020) 2130–2140.
[13] Q. Wu, W. Li, J. Zhao, et al., Biomed. Pharmacother. 137 (2021) 111308.
[14] Y. Hu, Y. Wang, X. Wen, et al., Research 2020 (2020) 4087069.
[15] N. Li, T. Wang, N. Wang, M. Fan, X. Cui, Angew. Chem. Int. Ed. 62 (2023) e202217326.
[16] Y. Zhang, Y. Zhang, Y. Yue, et al., Chin. Chem. Lett. 32 (2021) 2873–2876.
[17] W. Liu, J. Chen, Q. Qiao, X. Liu, Z. Xu, Chin. Chem. Lett. 33 (2022) 4943–4947.
[18] F. Wang, Y. Liu, B. Wang, et al., Dyes Pigm. 152 (2018) 29–35.
[19] M. Tian, X. Liu, H. He, et al., Anal. Chem. 92 (2020) 10068–10075.
[20] M. Tian, Y. Liu, F. Jiang, Anal. Chem. 92 (2020) 14285–14291.
[21] Y. Su, B. Yu, S. Wang, H. Cong, Y. Shen, Biomaterials 271 (2021) 120717.
[22] Y. Pan, S. Lei, J. Zhang, et al., Anal. Chem. 93 (2021) 17103–17109.
[23] Y. Zhang, J. Fang, S. Ye, et al., Nat. Commun. 13 (2022) 1685.
[24] S. Lei, F. Zhao, J. Zhang, et al., Anal. Chem. 94 (2022) 8399–8408.
[25] F. Zhao, X. Zhang, F. Bai, et al., Adv. Mater. 35 (2023) 2208097.
[26] Y. Guo, Z. Li, B. Guo, B. Wang, Y. Tu, Nano Biomed. Eng. 16 (2024) 135–151.
[27] Q. Lan, P. Yu, K. Yan, et al., J. Am. Chem. Soc. 144 (2022) 21010–21015.
[28] X. Zhang, Y. Chen, H. He, et al., Angew. Chem. Int. Ed. 60 (2021) 26337–26341.
[29] S. Bi, X. Wen, G. Sun, S. Zeng, Nano Today 53 (2023) 102027.
[30] L. Nie, X. Chen, Chem. Soc. Rev. 43 (2014) 7132–7170.
[31] X. Li, J. Kim, J. Yoon, X. Chen, Adv. Mater. 29 (2017) 1606854.
[32] Y. Liu, L. Teng, B. Yin, et al., Chem. Rev. 122 (2022) 6850–6918.
[33] E.Y. Zhou, H.J. Knox, C.J. Reinhardt, et al., J. Am. Chem. Soc. 140 (2018) 11686–11697.
[34] Y. Cui, X. Wang, Z. Jiang, et al., Angew. Chem. Int. Ed. 135 (2023) e202214505.
[35] C. Moore, Y. Cheng, N. Tjokro, et al., Angew. Chem. Int. Ed. 61 (2022) e202201843.
[36] Q. Fu, R. Zhu, J. Song, H. Yang, X. Chen, Adv. Mater. 31 (2019) 1805875.
[37] X. Gao, G. Ma, C. Jiang, et al., Anal. Chem. 91 (2019) 7112–7117.
[38] L. Yin, H. Sun, H. Zhang, et al., J. Am. Chem. Soc. 141 (2019) 3265–3273.
[39] L. Wu, Y. Ishigaki, W. Zeng, et al., Nat. Commun. 12 (2021) 6145.
[40] Z. Zeng, S.S. Liew, X. Wei, K. Pu, Angew. Chem. Int. Ed. 60 (2021) 26454–26475.
[41] Y. Ma, L. Xu, B. Yin, et al., Nano Lett. 21 (2021) 4484–4493.
[42] X. Zhang, K. Jiang, S. Jiang, et al., Anal. Chem. 94 (2022) 13770–13776.
[43] Y. Zhang, S. He, C. Xu, et al., Angew. Chem. Int. Ed. 61 (2022) e202203184.